

# Geophysical Research Letters®

## RESEARCH LETTER

10.1029/2024GL108263

### Special Collection:

Advancing Interpretable AI/ML Methods for Deeper Insights and Mechanistic Understanding in Earth Sciences: Beyond Predictive Capabilities

### Key Points:

- Gaps in satellite-derived land surface temperature (LST) measurements caused due to clouds can be tackled using graph-based propagation
- The proposed approach, GraphProp, recovers missing LST values more accurately than existing tensor completion methods from literature
- The presented results show the approach to be robust in even highly challenging settings including up to 90% cloud cover

### Supporting Information:

Supporting Information may be found in the online version of this article.

### Correspondence to:

I. Rolland,  
[imr27@cam.ac.uk](mailto:imr27@cam.ac.uk)

### Citation:

Rolland, I., Selvakumaran, S., Ahmad Shaikh, S. F. E., Hamel, P., & Marinoni, A. (2024). Improving land surface temperature estimation in cloud cover scenarios using graph-based propagation. *Geophysical Research Letters*, *51*, e2024GL108263. <https://doi.org/10.1029/2024GL108263>




Received 30 MAR 2024

Accepted 15 NOV 2024

© 2024. The Author(s).

This is an open access article under the terms of the [Creative Commons Attribution License](https://creativecommons.org/licenses/by/4.0/), which permits use, distribution and reproduction in any medium, provided the original work is properly cited.

## Improving Land Surface Temperature Estimation in Cloud Cover Scenarios Using Graph-Based Propagation

Iain Rolland<sup>1</sup> , Sivasakthy Selvakumaran<sup>1</sup>, Shaikh Fairul Edros Ahmad Shaikh<sup>2</sup> , Perrine Hamel<sup>2</sup> , and Andrea Marinoni<sup>1,3</sup>

<sup>1</sup>University of Cambridge, Department of Engineering, Cambridge, UK, <sup>2</sup>Nanyang Technological University, Asian School of the Environment, Singapore, Singapore, <sup>3</sup>UiT the Arctic University of Norway, Department of Physics and Technology, Tromsø, Norway

**Abstract** Land surface temperature (LST) serves as an important climate variable which is relevant to a number of studies related to energy and water exchanges, vegetation growth and urban heat island effects. Although LST can be derived from satellite observations, these approaches rely on cloud-free acquisitions. This represents a significant obstacle in regions which are prone to cloud cover. In this paper, a graph-based propagation method, referred to as GraphProp, is introduced. This method can accurately obtain LST values which would otherwise have been missing due to cloud cover. To validate this approach, a series of experiments are presented using synthetically obscured Landsat acquisitions. The validation takes place over scenarios ranging from between 10% and 90% cloud cover across six urban locations. In presented experiments, GraphProp recovers missing LST values with a mean absolute error of less than 1.1°C, 1.0°C and 1.8°C in 90% cloud cover scenarios across the studied locations respectively.

**Plain Language Summary** Although it is possible to work out what the ground temperature is from satellite images, when there are clouds which cover part of the image we cannot use existing methods. In parts of the world which are often cloudy, this means you might only occasionally have access to information about the surface temperature. Land surface temperature relates to many physical processes, therefore, we propose a method which aims to provide accurate surface temperature values even when it is cloudy, in order to assist the study of these systems. To do so, the method we propose uses a satellite image of the same region which was captured on a different day when there were not clouds. This earlier image is used to describe the region in a graph structure, where similar areas are grouped together. This representation of the region is then used to work out what the region might have looked like if there were not clouds in the later image. From this, we can apply existing methods to compute the land surface temperature. In our experiments we show that this approach is effective and the recovered temperature values are more accurate than can be recovered by other existing approaches.

## 1. Introduction

Land Surface Temperature (LST) has been identified as an Essential Climate Variable (ECV) by the Global Climate Observing System (Zemp et al., 2022). It is relevant to many phenomena that characterize Earth's climate including urban heat island effects (Morabito et al., 2016; Nazarian et al., 2022; Zhou et al., 2018), water exchanges (Anderson et al., 2016; Knipper et al., 2019) and vegetation health (Bento et al., 2018; Masitoh & Rusydi, 2019). LST can be estimated using passive microwave measurements (Dowling et al., 2021; Holmes et al., 2009; Zhao et al., 2017) and integration of records from geostationary observations (Zhu et al., 2022; Q. Wang et al., 2024). In regions of persistent cloud cover, however, LST rasters often contain missing data. LST calculations rely on measured thermal infrared (TIR) energy emitted from the surface (Wan & Dozier, 1996), with clouds preventing such measurements. Given the importance of LST as an ECV, it is important to overcome these barriers to allow for the subsequent study of the processes to which it pertains.

Two types of LST reconstruction exist in literature: clear-sky and all-sky reconstruction. Clear-sky reconstruction methods estimate the measurement which would have been made in the absence of clouds, whereas all-sky methods estimate what an in-situ sensor underneath the clouds would have measured. In this work, we present a method which performs clear-sky reconstruction. Although there is evidence that LST data sets consisting of only clear-sky values may exhibit biases (Ermida et al., 2019; Xu et al., 2023), having methods capable of accurately estimating clear-sky values is also important. As well as serving as inputs for a number of all-sky LST

reconstruction methods (Yao et al., 2023), reconstructed clear-sky LST values have also been used to assist a number of application studies (Leihy et al., 2018; Li et al., 2020; Yang et al., 2020).

Existing clear-sky LST reconstruction methods can be categorized into one of two groupings: model-based methods or statistical methods (Mo et al., 2021). Within the former, temperature cycle models including Quan et al. (2016); Sobrino and Julien (2013); Fu and Weng (2015); Zhan et al. (2014); Mohanasundaram et al. (2023) work by constructing physical models of the temperature fluctuations with parameters fit to available observations. Although these models can be used to estimate continuous LST time series, they struggle to capture spatial variability and higher frequency temperature dynamics. In Zou et al. (2018), although the authors propose a model-based approach which aims to better capture short-term LST fluctuations, they acknowledge that the approach struggles in built-up regions.

In the statistical category of methods, a number of methods have been proposed for LST reconstruction (Mo et al., 2021). These range in their sophistication from simple imputation methods such as mean filling or linear interpolation to more rigorous methods such as tensor completion methods. Although not directly studied for reconstructing cloud-obfuscated LST values, tensor completion methods including Ng et al. (2017); Srindhuna and Baburaj (2020); He et al. (2019); Y. Chen et al. (2019) have been proposed to address cloud-covered acquisitions. These methods operate under the assumption that the data is low rank and completes the missing regions so as to satisfy this assumption. In studies which consider the limits of recoverability for these methods, they generally assume that observations are randomly distributed (Ashraphijuo et al., 2017). This does not typically hold for cloud-obfuscated data, where missing regions generally form contiguous regions, which these methods struggle to recover (Rolland et al., 2023).

In this manuscript, we adopt a graph-based propagation approach which reconstructs missing LST values more accurately than methods in existing literature. The adopted approach avoids LST gaps by completing the missing inputs used to compute LST (Rolland et al., 2023). The major advantage of tackling the problem upstream in this way is that the physics which are embedded within the downstream LST equations are utilized fully and therefore any results remain physically consistent. Methods which tackle the gaps at the output stage do not have this same guarantee.

Presented results validate the proposed approach by performing experiments using synthetically introduced gaps within a Landsat data set. This allows for the quality of the LST outputs to be assessed against the LST values computed using the original data. The GraphProp approach is shown to more accurately reconstruct missing LST values than benchmarked completion methods and is shown to do so in even extreme cloud cover scenarios where 90% of the image is obscured.

## 2. Materials and Methods

### 2.1. GraphProp Completion

The proposed approach tackles the problem of filling the gaps in the LST raster by tackling the gaps in the Landsat inputs. The intermediate product of this approach is a fully reconstructed raster depicting what would have been observed under clear-sky conditions. This allows the Statistical Mono-Window (SMW) algorithm to be used. The GraphProp method has been developed to perform remote sensing image completion and has been rigorously tested for that task (Rolland et al., 2023). In this study, we extend this work by considering the method's suitability for this application scenario by assessing the accuracy of LST values derived from the method's outputs.

To obtain a cloud-free raster, GraphProp constructs a graph-based representation of the region. A graph,  $\mathcal{G}$ , consists of a node set,  $\mathcal{V}$ , and an edge set,  $\mathcal{E}$ , with edges connecting two nodes. In the context of this study, edges are used to connect pixels that exhibited similarity.

The GraphProp method uses an earlier cloud-free acquisition to construct the graph-based representation of the region. Using  $\mathcal{H}^0$  and  $\mathcal{H}^1$  to denote the reference and partially observed rasters with three dimensions respectively (having shape  $H \times W \times C$  where  $H$ ,  $W$  and  $C$  are the height, width and number of image channels respectively), the graph is constructed as follows. By indexing the first two dimensions, that is, both spatial dimensions,

$\mathcal{H}^0[i, j, :]$ , we reference a specific pixel and obtain a vector of length  $C$  containing the pixel's spectral signature. Since the reference acquisition is cloud-free, we can do so for all pixels to obtain a  $HW$  vectors in  $C$ -dimensional space. In this application, the following nine Landsat 8 bands are used: the first seven surface reflectance bands (from ultra blue to shortwave infrared); and top of atmosphere bands 10 and 11 (thermal infrared). The graph-based representation of the region is constructed using a  $k$ -nearest neighbors graph. By introducing an edge between a node and its  $k$ -nearest neighbors, a graph is obtained. This graph provides the structure upon which the observations from the partially observed acquisition are propagated.

The values which are propagated are the spectral signatures from the cloud-obscured acquisition. This removes any strict requirement for the signatures to remain close across the two acquisitions, allowing the dynamic nature of surface spectral signals to be handled.

The assumption made by adopting this approach is that pixels which were observed to exhibit similarity in the reference image are likely to also exhibit similarity in the partially observed acquisition. The two images will ideally have been captured within a short time frame to ensure this assumption holds. The presented results suggest that the method can be applied even over longer time frames, provided the area has not undergone significant changes in land cover between acquisitions. The method cannot, for example, account for an area which was deforested or urbanized between acquisitions.

To mathematically describe the propagation the following notation is used. First, a function  $\text{FSD}(\cdot)$ , short for Flattening Spatial Dimensions, is defined. It reduces a raster of three dimensions into a matrix by flattening the spatial dimensions, giving  $\mathbf{F}^0 = \text{FSD}(\mathcal{H}^0) \in \mathbb{R}^{HW \times C}$  and  $\mathbf{F}^1 = \text{FSD}(\mathcal{H}^1) \in \mathbb{R}^{HW \times C}$ . The inverse Unflattening Spatial Dimensions operation is also defined,  $\text{USD}(\cdot)$ , such that  $\mathcal{H}^1 = \text{USD}(\mathbf{F}^1)$ . A mask,  $\Omega$ , is defined to index the pixels that were observed in the cloud-obscured acquisition, such that  $\mathbf{F}_{\Omega}^1$  gives the matrix with only the rows of  $\mathbf{F}^1$  corresponding to observed pixels. The complement set,  $\Omega_c$ , is used to define the missing pixels, such that  $\mathbf{F}_{\Omega_c}^1$  contains the entries to be recovered.

In this notation, the finite difference approximation to heat diffusion on a graph, as described by Kondor and Lafferty (2002), is expressed using the graph's Laplacian matrix,  $\mathbf{L}$ , as

$$\frac{\partial \mathbf{F}^1}{\partial t} \propto -\mathbf{L}\mathbf{F}^1. \quad (1)$$

Diffusion provides a steady-state solution where each node converges toward the feature average of its immediate graph neighbors. To avoid oversmoothing, the diffusion equation is modified to hold observed entries fixed. This is achieved by considering the temporal derivative as zero for these rows in  $\mathbf{F}^1$ . The Laplacian is indexed by its rows and columns such that  $\mathbf{L}_{\Omega\Omega_c}$  denotes the submatrix consisting of the rows corresponding to observed pixels and the columns corresponding to the missing pixels.

This allows us to represent the propagation for the unobserved rows in  $\mathbf{F}^1$  as

$$\frac{\partial \mathbf{F}_{\Omega_c}^1}{\partial t} \propto -\mathbf{L}_{\Omega_c\Omega}\mathbf{F}_{\Omega}^1 - \mathbf{L}_{\Omega_c\Omega_c}\mathbf{F}_{\Omega_c}^1. \quad (2)$$

The steady state can be found either by iteratively applying steps proportional to the derivative in (Equation 2) or by setting the derivative to zero and obtaining  $\mathbf{F}_{\Omega_c}^1$  as the solution to

$$\mathbf{L}_{\Omega_c\Omega_c}\mathbf{F}_{\Omega_c}^1 = -\mathbf{L}_{\Omega_c\Omega}\mathbf{F}_{\Omega}^1. \quad (3)$$

The implementation steps of GraphProp are summarized in Algorithm 1. The method has only one parameter, the number neighbors,  $k$ , which was set to 25 in the conducted experiments following preliminary testing (presented in Supporting Information S1).

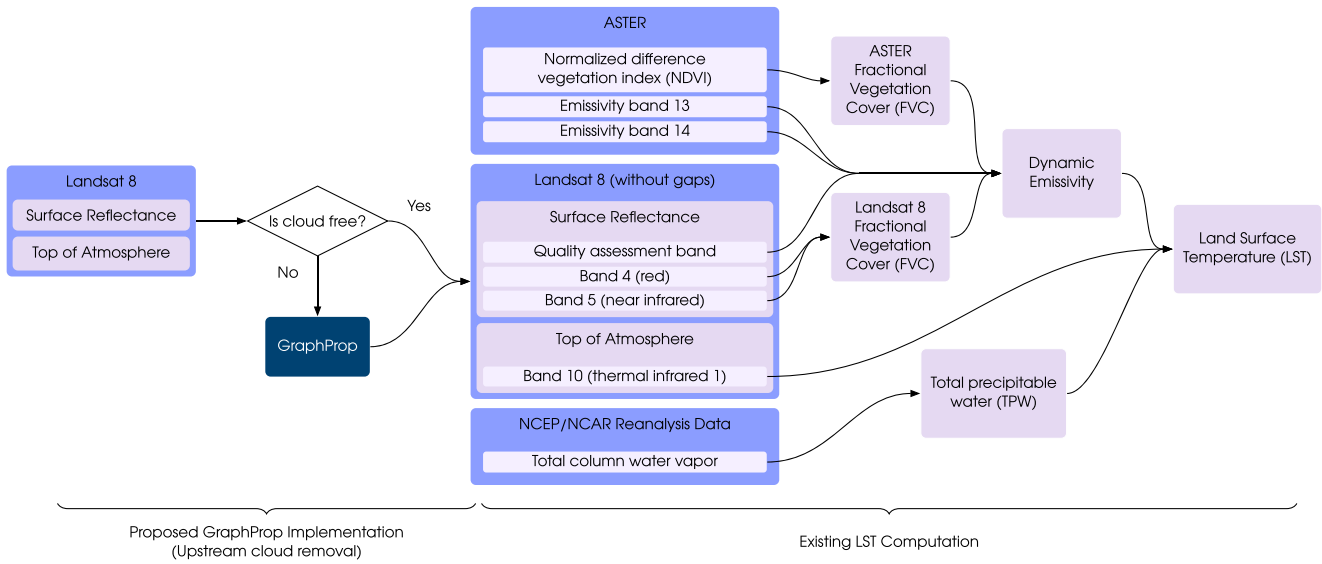


**Figure 1.** Schematic showing how the proposed approach integrates with existing algorithm for computing LST (Ermida et al., 2020). The advantage of adopting an upstream completion approach is that it does not alter the physics that relate measured thermal infrared energy to LST.

---

**Algorithm 1.** GraphProp Algorithm

---

**Input:**  $\Omega, \mathcal{H}^0, \mathcal{H}_c^1$  ▷ Observation mask, reference input, partially observed input

1:  $\mathbf{F}^0 = \text{FSD}(\mathcal{H}^0) \in \mathbb{R}^{HW \times C}$  ▷ Flatten reference input

2:  $\mathbf{F}_c^1 = \text{FSD}(\mathcal{H}_c^1) \in \mathbb{R}^{HW \times C}$  ▷ Flatten partially observed input

3:  $\mathcal{E} \leftarrow \text{kNN}(\mathbf{F}^0)$  ▷  $k$ -nearest neighbors graph (using reference input)

4:  $\mathbf{L} = \text{Laplacian}(\mathcal{E})$  ▷ Laplacian matrix of graph

5:  $\mathbf{F}_{\Omega_c}^1 \leftarrow \text{Solve}(\mathbf{L}_{\Omega_c \Omega_c} \mathbf{F}_{\Omega_c}^1 = -\mathbf{L}_{\Omega_c \Omega} \mathbf{F}_{\Omega}^1)$  ▷ Solve diffusion for missing entries

6:  $\mathcal{H}^1 = \text{USD}(\text{Merge}(\mathbf{F}_{\Omega}^1, \mathbf{F}_{\Omega_c}^1))$

**Output:**  $\mathcal{H}^1$

---

**2.2. LST Calculations**

The SMW algorithm allows LST values to be calculated from a satellite's TIR band. The SMW models use coefficients obtained by fitting linear regression models that relate measured 11  $\mu\text{m}$  radiance values and the total column water vapor (TCWV) to LST. These coefficients can then be used to map the satellite-derived inputs to a LST value which would be measured at that location. This approach is adopted by Ermida et al. (2020), where they integrate the process into the Google Earth Engine (GEE) platform. The algorithm provided in GEE by Ermida et al. (2020) is depicted in Figure 1.

In addition to the TIR measurements captured by Landsat 8's Band 10, a number of other inputs are used. First, a dynamic estimation of the ground's emissivity is obtained, where emissivity is the ratio of energy emitted to the amount which a black body would emit in equivalent conditions. To estimate this quantity dynamically, the Landsat acquisition is used to obtain an instantaneous measure of fractional vegetation cover (FVC), a quantity describing the fraction of total area covered by vegetation. This value is used to update the static measure of FVC, obtained using the ASTER Global Emissivity Data set. Additionally, NCEP/NCAR Reanalysis Data is used to quantify the precipitable water in the atmosphere. Through quantification of TCWV and subsequently the total precipitable water (TPW), the effect that the atmosphere has on the measured brightness temperatures is accounted for (Ermida et al., 2020).

The primary cause of missing LST values is the presence of clouds. Since the SMW algorithm depicted in Figure 1 is applied in a pixel-wise fashion, in scenes that are obscured, the gaps in the LST output match the cloud pattern.

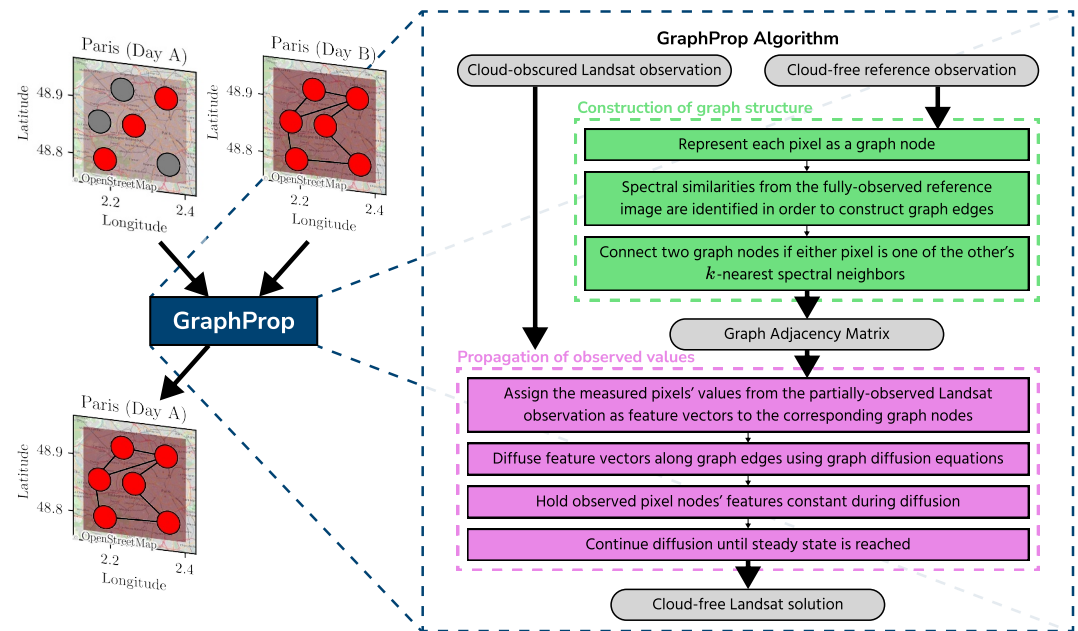


**Figure 2.** Overview of the GraphProp method. The graph structure is used to propagate observed values (denoted by red nodes) to complete missing values (denoted by gray nodes).

### 2.3. Experimental Design

Experiments involving synthetically obscured data have been performed to assess the accuracy of LST reconstruction. This involved the creation of a cloud-free data set of observations upon which the SMW algorithm was used to compute reference LST values. As GraphProp involves exploiting an earlier acquisition of the region, the data set consists of cloud-free image pairs.

In this study, six urban locations were selected: Jakarta, London, Paris, Cairo, Gaborone, and Québec City. Urban locations were selected as the primary focus of the study as they exhibit smaller scale land cover heterogeneities that result in localized LST variations (Xiao et al., 2007) and therefore represent a challenging gap-filling task. The cities fall within the following Köppen climate groups (Beck et al., 2018): Jakarta (Am), London (Cfb), Paris (Cfb), Cairo (BWh), Gaborone (BSh), and Québec City (Dfb). They were selected from different climate types to allow a diverse range of temperature dynamics to be tested.

In each of the six cities, the region of interest covers a square with side length 20 km and acquisitions were acquired at a resolution of 30 m per pixel. Within each region's image pair the earlier acquisition acts as the cloud-free reference image. The temporal gap between acquisitions varies for each city, ranging from 2 to 20 weeks. These temporal gaps are representative of the temporal separation one might expect in real-world applications of the proposed approach.

In order to realistically synthetically obscure the latter acquisitions, genuine cloud masks from other cloud-obscured acquisitions were collected. These masks represent cloud cover scenarios which range from 10%-90% cloud cover. At each of these 10% intervals, 10 masks were collected, totaling 90 masks.

### 2.4. Evaluation

To quantify the accuracy of each method's recovered LST values, the mean absolute error (MAE) was computed over the missing regions of each scene. Using  $f(\cdot)$  to summarize the function for deriving LST from the satellite data, MAE is defined below. The algorithm-recovered LST values are contained within the matrix  $\overline{\text{LST}}$ , where

$$\overline{\text{LST}} = f(\mathcal{H}^I) \in \mathbb{R}^{H \times W}.$$

By flattening the spatial dimensions of the LST matrix, a vector of LST values can be obtained,  $\overline{\text{LST}}_{\text{flat}}$ , where

$$\overline{\text{LST}}_{\text{flat}} = \text{FSD}(\text{LST}) \in \mathbb{R}^{HW},$$

and then indexed using  $\Omega_c$  to consider only the missing regions of the matrix:

$$(\overline{\text{LST}}_{\text{flat}})_{\Omega_c} \in \mathbb{R}^{|\Omega_c|}.$$

By comparing against the ground truth, in the matrix LST, the MAE was computed as follows:

$$\text{MAE} = \frac{\|(\overline{\text{LST}}_{\text{flat}})_{\Omega_c} - (\text{LST}_{\text{flat}})_{\Omega_c}\|_1}{|\Omega_c|},$$

where  $\|\cdot\|_2$  and  $\|\cdot\|_1$  are the  $l_2$  and  $l_1$  norms respectively.

Presented errors are computed against the values obtained using the SMW algorithm when taking the synthetically obscured pixel values as inputs.

## 2.5. Benchmarked Methods

### 2.5.1. Mean-Filled LST

The first benchmarked method uses an approach which takes the partially computed LST raster and fills gaps with the mean of the computed values. This baseline provides a commonly adopted approach, frequently used for its simplicity. In literature this is similar to as seen in T. Wang et al. (2019), where they differ slightly by using mean interpolation from sliding window regions.

### 2.5.2. Band-Wise Mean-Filled Landsat Inputs

Rather than imputation using the average LST value, a second baseline approach is provided by mean-filling the inputs. Techniques of this form have been used to recover gaps in Landsat images in other remote sensing applications (J. Chen et al., 2023; Zhang et al., 2021). Here, the mean observed value for each band is computed and used to fill each band's missing entries. The SMW algorithm is applied to the mean-filled inputs to obtain a gap-free LST raster.

### 2.5.3. Low-Rank Tensor Completion

A third baseline approach takes a more rigorous approach to the problem of missing data. The low-rank tensor completion approach is based on the assumption that the data can be represented by a low-rank tensor.

There have been many studies which present tensor completion algorithms which make this assumption (Cai et al., 2010; He et al., 2019; Liu et al., 2013; Yuan et al., 2019) to recover missing entries.

In this study, the high accuracy low rank tensor completion algorithm (HaLRTC) (Liu et al., 2013) provides a benchmark from this family of methods. It was applied by stacking the partially observed top of atmosphere B10 band with the two surface reflectance bands used to compute LST (SR\_B4 and SR\_B5). Results were obtained using the author-recommended parameter settings for the algorithm.

### 2.5.4. Time-Series Models

Additionally, there exist the approaches to LST imputation that use model-based methods. In particular, we consider the pixel-wise multiple linear regression model (PMLR) proposed by Mohanasundaram et al. (2023). This method requires a full year of observations to fit the model and so additional observations were obtained to fairly apply this approach. The method fits parameterized functions in order to model NDVI variations and to relate NDVI to LST values. When a pixel is missing due to cloud cover, the pixel-specific functions which have been fitted are used to estimate the NDVI value which is then used to obtain an estimate for the LST measurement.

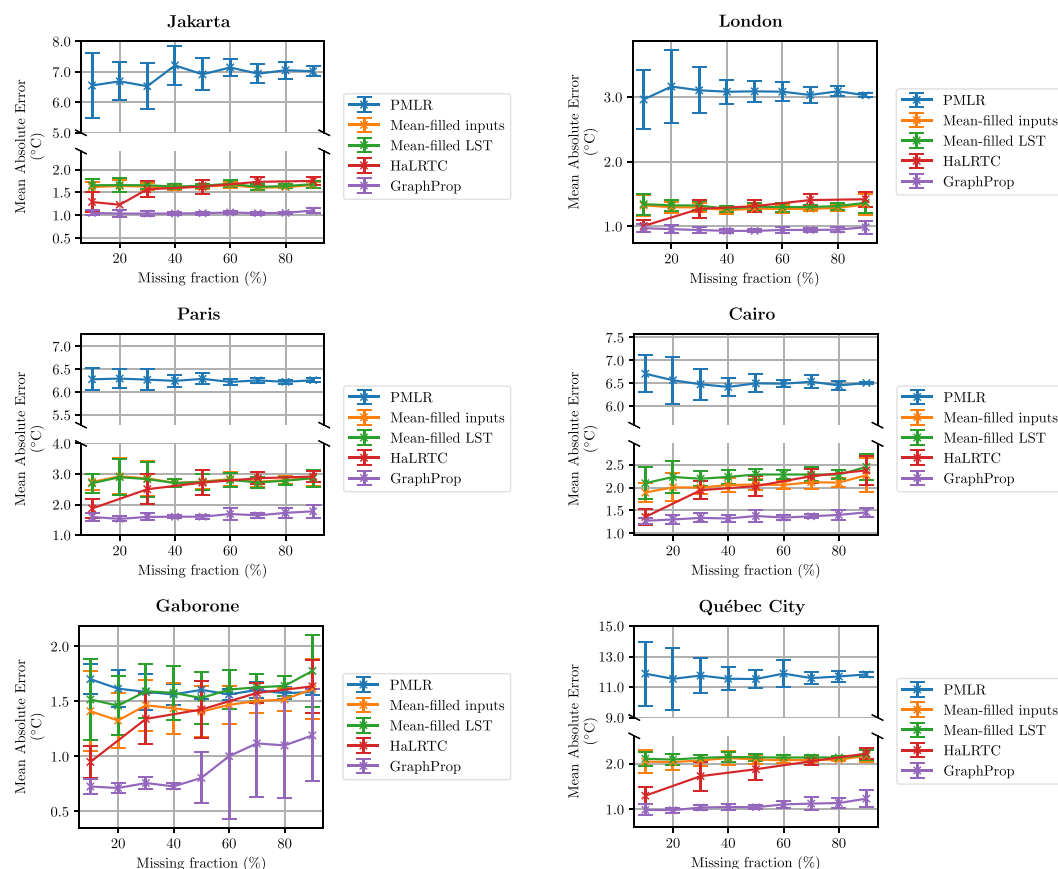


**Figure 3.** Accuracy of completed LST values as a function of the percentage of the acquisition removed. Plotted values represents the mean value across 10 random obfuscation masks and error bars represent plus-or-minus one standard deviation.

### 3. Results

#### 3.1. Validation Using Synthetically Obscured Data

Applying a cloud mask to synthetically obscure the latter image from each pair, each method is applied to reconstruct missing LST values. Doing so for 10 cloud masks between 10%–90% cloud cover at 10% intervals, the MAE was computed for each method. The results, shown in Figure 3, show the mean value when the MAE values are averaged over the 10 cloud masks at a given cloud cover fraction. The errors are computed over the missing pixels in each experiment only and not over the whole scene, since the errors are zero or negligible when observed.

Across the six cities studied, the low-rank tensor completion method (HaLRTC) provides improved accuracy versus the mean-filling approaches when cloud cover is minimal, that is, in the region of 10%–30%. When more severely cloud-obscured, mean-filling provides equally or more accurate results. This could perhaps be explained by the fact that as cloud cover increases, the large contiguous missing regions deviate further from the founding assumption of low-rank completion approaches that consider entries to be missing randomly.

The time-series model (PMLR) provides particularly poor results in all locations other than Gaborone. This is likely due to the method's assumption that a correlation exists between NDVI and LST. In the urban locations studied, this correlation is likely weak or non-existent. Therefore, PMLR struggles to handle seasonal variations, despite using more input acquisitions than other tested methods.

However, the proposed method, summarized in Figure 2, improves the LST accuracy across all cloud cover fractions. GraphProp provides an average MAE of less than 1.1°C, 1.0°C, 1.8°C, 1.5°C, 1.2°C and 1.3°C across

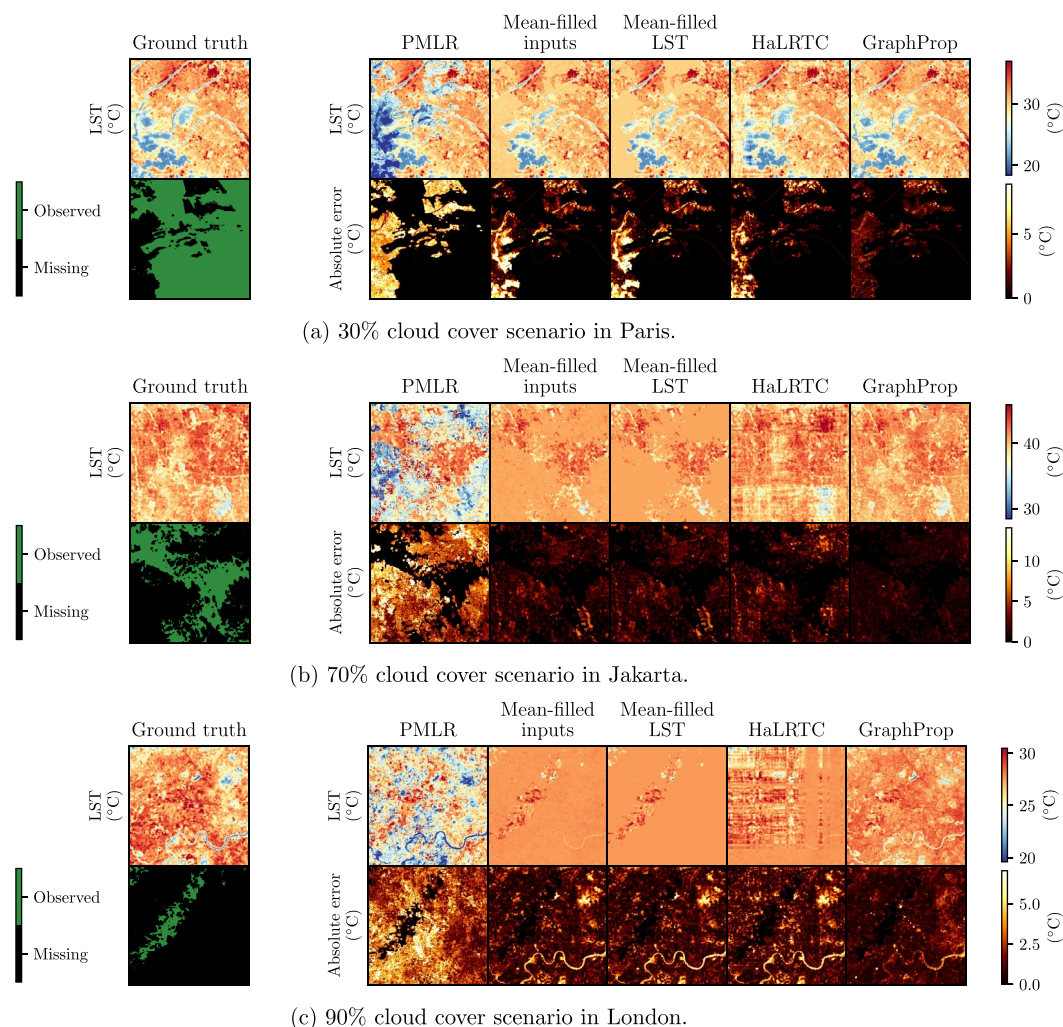


**Figure 4.** Qualitative comparison of methods for varying amounts of cloud cover.

all tested scenarios in Jakarta, London, Paris, Cairo, Gaborone and Québec City respectively. Results do not show a significant deterioration in accuracy as cloud cover increases, unlike in results from HaLRTC.

A selection of results are displayed in Figure 4 illustrating the spatial accuracy characteristics of each method. These absolute error distributions demonstrate that GraphProp can recover fine-scale LST variations more accurately than other methods and therefore gives results with fewer neighborhoods of high error magnitude.

### 3.2. Working With Real Cloud-Obfuscated Data

To consider the performance of GraphProp when applied to real cloud-obscured data, a short qualitative analysis is presented. In Figure 5, a cloud-obscured scene from Jakarta is considered. Here, the cloud mask has been derived from the quality assessment (QA) band. The cloud-masked acquisition in Figure 5a shows a few pixels from cloud edges have not been labeled correctly in the QA band. The results show GraphProp applied treating these pixels as though they were “observed”.

This issue can be mitigated by applying a binary dilation operation (Todorov et al., 2023) to the cloud mask. The results obtained using this approach can be seen in Figure 5b.

Although there is some compromise in accuracy without performing mask dilation, the errors appear to remain mainly localized to the cloud edges. This suggests an encouraging robustness against this imperfection of real-



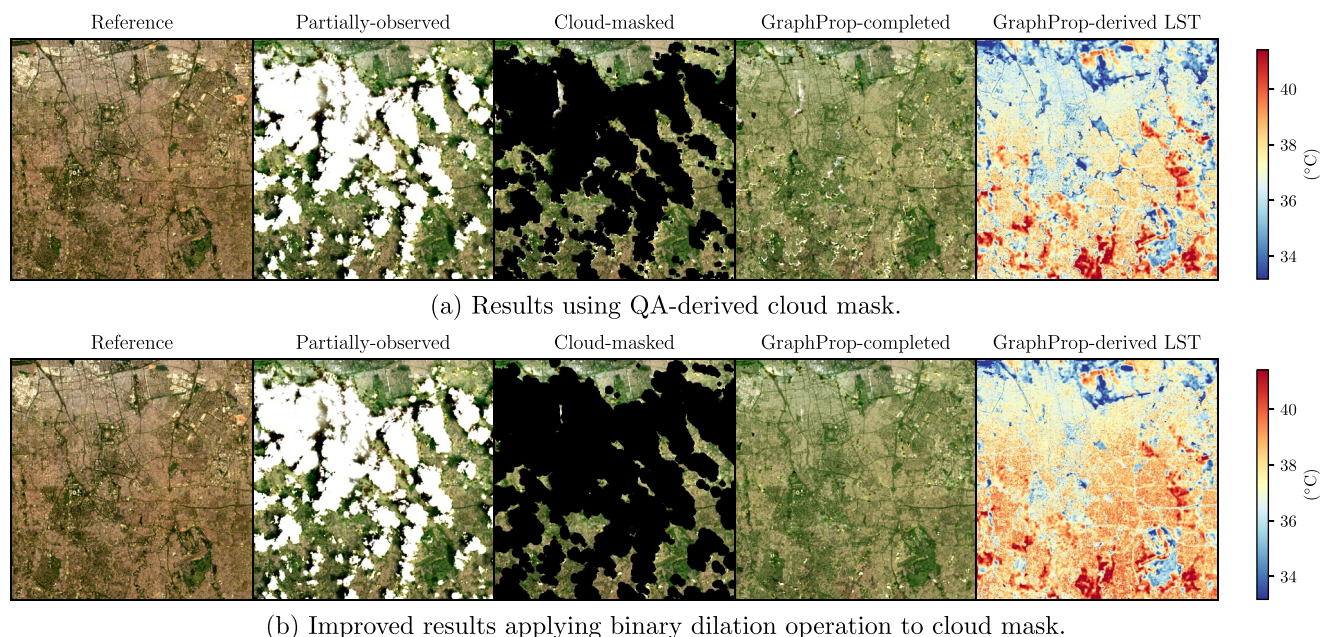


**Figure 5.** Application to real cloud-obscured Jakarta scene where the QA-derived cloud mask imperfectly captures cloud edges.

world data. With the suggested mask dilation, however, the cloud edges are better captured which should improve accuracy.

#### 4. Discussion and Conclusions

The results presented show the proposed method, GraphProp, reconstructs accurate LST values. It is important that LST reconstructions are accurate given the direct implications they have on tasks such as energy resource planning and management. It has been estimated (Santamouris et al., 2015) that each 1°C increase in temperature within urban heat islands can increase energy demands by between 0.5-5%.

The presented method provides more accurate results than the benchmarked low-rank tensor completion method (HaLRTC), mean-filling approaches, as well as the state of the art from time-series modeling approaches (PMLR). Results also show this approach to be robust against the extent of cloud cover present in the scene. The contribution, therefore, represents a useful and practical tool for recovering clear-sky LST values. This will assist applications involving the analysis of LST dynamics, by reducing gaps in time series caused by cloud cover and therefore provide a more complete picture of temporal trends.

This study has focused on urban areas, however the authors expect similar results to be achievable if applied to other land cover types. The method can also be straightforwardly extended to time series involving more than two acquisitions, for example, by combining graphs obtained from each. This would allow for the case where it is not required that any one of the reference acquisitions is fully cloud-free, provided that each location is observed without cloud in at least one of the acquisitions to identify its spectral similarities allowing it to be incorporated into the graph-based representation of the region.

There is scope to extend this research to analyze how the accuracy of the proposed approach varies as other variables such as the temporal or seasonal distance between the respective acquisitions is changed.

#### Data Availability Statement

The data were obtained using Google Earth Engine (<https://earthengine.google.com/>). The code used is available in (Rolland, 2024).

**Acknowledgments**

This work was funded through the following sources: the UK Engineering and Physical Sciences Research Council (EPSRC) [grant number EP/T517847/1]; Visual Intelligence Centre for Research-based Innovation funded by the Research Council of Norway [RCN Grant 309439]; the NATALIE project funded by the European Union Horizon Europe Climate research and innovation program under grant agreement no. 101112859; the Climate Transformation Program funded by the Ministry of Education of Singapore; the Isaac Newton Trust; and Newnham College, Cambridge, United Kingdom.

**References**

Anderson, M. C., Zolin, C. A., Sentelhas, P. C., Hain, C. R., Semmens, K., Yilmaz, M. T., et al. (2016). The evaporative stress index as an indicator of agricultural drought in Brazil: An assessment based on crop yield impacts. *Remote Sensing of Environment*, *174*, 82–99. <https://doi.org/10.1016/j.rse.2015.11.034>

Ashraphijoo, M., Aggarwal, V., & Wang, X. (2017). On deterministic sampling patterns for robust low-rank matrix completion. *IEEE Signal Processing Letters*, *25*(3), 343–347. <https://doi.org/10.1109/lsp.2017.2780983>

Beck, H. E., Zimmermann, N. E., McVicar, T. R., Vergopolan, N., Berg, A., & Wood, E. F. (2018). Present and future Köppen-Geiger climate classification maps at 1-km resolution. *Scientific Data*, *5*(1), 1–12. <https://doi.org/10.1038/sdata.2018.214>

Bento, V. A., Gouveia, C. M., DaCamara, C. C., & Trigo, I. F. (2018). A climatological assessment of drought impact on vegetation health index. *Agricultural and Forest Meteorology*, *259*, 286–295. <https://doi.org/10.1016/j.agrformet.2018.05.014>

Cai, J.-F., Candès, E. J., & Shen, Z. (2010). A singular value thresholding algorithm for matrix completion. *SIAM Journal on Optimization*, *20*(4), 1956–1982. <https://doi.org/10.1137/080738970>

Chen, J., Huang, J., Zhang, X., Chen, J., & Chen, X. (2023). Monitoring total suspended solids concentration in Poyang Lake via machine learning and Landsat images. *Journal of Hydrology: Regional Studies*, *49*, 101499. <https://doi.org/10.1016/j.ejrh.2023.101499>

Chen, Y., He, W., Yokoya, N., & Huang, T.-Z. (2019). Blind cloud and cloud shadow removal of multitemporal images based on total variation regularized low-rank sparsity decomposition. *ISPRS Journal of Photogrammetry and Remote Sensing*, *157*, 93–107. <https://doi.org/10.1016/j.isprsjprs.2019.09.003>

Dowling, T. P., Song, P., Jong, M. C. D., Merbold, L., Wooster, M. J., Huang, J., & Zhang, Y. (2021). An improved cloud gap-filling method for longwave infrared land surface temperatures through introducing passive microwave techniques. *Remote Sensing*, *13*(17), 3522. <https://doi.org/10.3390/rs13173522>

Ermida, S. L., Soares, P., Mantas, V., Götsche, F.-M., & Trigo, I. F. (2020). Google Earth engine open-source code for land surface temperature estimation from the landsat series. *Remote Sensing*, *12*(9), 1471. <https://doi.org/10.3390/rs12091471>

Ermida, S. L., Trigo, I. F., DaCamara, C. C., Jiménez, C., & Prigent, C. (2019). Quantifying the clear-sky bias of satellite land surface temperature using microwave-based estimates. *Journal of Geophysical Research: Atmospheres*, *124*(2), 844–857. <https://doi.org/10.1029/2018jd029354>

Fu, P., & Weng, Q. (2015). Temporal dynamics of land surface temperature from landsat tir time series images. *IEEE Geoscience and Remote Sensing Letters*, *12*(10), 2175–2179. <https://doi.org/10.1109/lgrs.2015.2455019>

He, W., Yokoya, N., Yuan, L., & Zhao, Q. (2019). Remote sensing image reconstruction using tensor ring completion and total variation. *IEEE Transactions on Geoscience and Remote Sensing*, *57*(11), 8998–9009. <https://doi.org/10.1109/TGRS.2019.2924017>

Holmes, T., De Jeu, R., Owe, M., & Dolman, A. (2009). Land surface temperature from Ka band (37 GHz) passive microwave observations. *Journal of Geophysical Research*, *114*(D4). <https://doi.org/10.1029/2008jd010257>

Knipper, K. R., Kustas, W. P., Anderson, M. C., Alfieri, J. G., Prueger, J. H., Hain, C. R., et al. (2019). Evapotranspiration estimates derived using thermal-based satellite remote sensing and data fusion for irrigation management in California vineyards. *Irrigation Science*, *37*(3), 431–449. <https://doi.org/10.1007/s00271-018-0591-y>

Kondor, R., & Lafferty, J. (2002). Diffusion kernels on graphs and other discrete input spaces. *ICML*, *2*.

Lei, R. I., Duffy, G. A., Nortje, E., & Chown, S. L. (2018). High resolution temperature data for ecological research and management on the Southern Ocean Islands. *Scientific Data*, *5*(1), 1–13. <https://doi.org/10.1038/sdata.2018.177>

Li, Y., Wang, X., Chen, Y., & Wang, M. (2020). Land surface temperature variations and their relationship to fractional vegetation coverage in subtropical regions: A case study in Fujian province, China. *International Journal of Remote Sensing*, *41*(6), 2081–2097. <https://doi.org/10.1080/01431161.2019.1685714>

Liu, J., Musialski, P., Wonka, P., & Ye, J. (2013). Tensor completion for estimating missing values in visual data. *IEEE Transactions on Pattern Analysis and Machine Intelligence*, *35*(1), 208–220. <https://doi.org/10.1109/TPAMI.2012.39>

Masitoh, F., & Rusydi, A. (2019). Vegetation health index (vhi) analysis during drought season in brantas watershed. *IOP Conference Series: Earth and Environmental Science*, *389*(1), 012033. <https://doi.org/10.1088/1755-1315/389/1/012033>

Mo, Y., Xu, Y., Chen, H., & Zhu, S. (2021). A review of reconstructing remotely sensed land surface temperature under cloudy conditions. *Remote Sensing*, *13*(14), 2838. <https://doi.org/10.3390/rs13142838>

Mohanasundaram, S., Baghel, T., Thakur, V., Udmale, P., & Shrestha, S. (2023). Reconstructing NDVI and land surface temperature for cloud cover pixels of Landsat-8 images for assessing vegetation health index in the Northeast region of Thailand. *Environmental Monitoring and Assessment*, *195*(1), 211. <https://doi.org/10.1007/s10661-022-10802-5>

Morabito, M., Crisci, A., Messeri, A., Orlandini, S., Raschi, A., Maracchi, G., & Munafò, M. (2016). The impact of built-up surfaces on land surface temperatures in Italian urban areas. *Science of the Total Environment*, *551*, 317–326. <https://doi.org/10.1016/j.scitotenv.2016.02.029>

Nazarian, N., Krayenhoff, E. S., Bechtel, B., Hondula, D. M., Paolini, R., Vanos, J., et al. (2022). Integrated assessment of urban overheating impacts on human life. *Earth's Future*, *10*(8), e2022EF002682. <https://doi.org/10.1029/2022EF002682>

Ng, M. K.-P., Yuan, Q., Yan, L., & Sun, J. (2017). An adaptive weighted tensor completion method for the recovery of remote sensing images with missing data. *IEEE Transactions on Geoscience and Remote Sensing*, *55*(6), 3367–3381. <https://doi.org/10.1109/TGRS.2017.2670021>

Quan, J., Zhan, W., Chen, Y., Wang, M., & Wang, J. (2016). Time series decomposition of remotely sensed land surface temperature and investigation of trends and seasonal variations in surface urban heat islands. *Journal of Geophysical Research: Atmospheres*, *121*(6), 2638–2657. <https://doi.org/10.1002/2015jd024354>

Rolland, I. (2024). IMPACTSquad/LST-gaps: LST-gaps. *Zenodo*. <https://doi.org/10.5281/zenodo.12731921>

Rolland, I., Selvakumaran, S., & Marinoni, A. (2023). Remote sensing image completion using a diffusion-based propagation algorithm. *Image and signal processing for remote sensing xxix*, *12733*, 57–66.

Santamouris, M., Cartalis, C., Synnefa, A., & Kolokotsa, D. (2015). On the impact of urban heat island and global warming on the power demand and electricity consumption of buildings—A review. *Energy and Buildings*, *98*, 119–124. <https://doi.org/10.1016/j.enbuild.2014.09.052>

Sobrino, J. A., & Julien, Y. (2013). Time series corrections and analyses in thermal remote sensing. In *Thermal infrared remote sensing: Sensors, methods, applications* (pp. 267–285). Springer.

Srindhuna, M., & Baburaj, M. (2020). Estimation of missing data in remote sensing images using t-svd based tensor completion. In *2020 international conference for emerging technology (incet)* (pp. 1–5).

Todorov, G., Docheva, L., Dochev, I., & Manev, S. (2023). Image processing methods for microorganisms adapted for laboratory exercises. In *2023 31st national conference with international participation (telecom)* (pp. 1–4). <https://doi.org/10.1109/TELECOMS59629.2023.10409654>

Wan, Z., & Dozier, J. (1996). A generalized split-window algorithm for retrieving land-surface temperature from space. *IEEE Transactions on Geoscience and Remote Sensing*, *34*(4), 892–905. <https://doi.org/10.1109/36.508406>

- Wang, Q., Tang, Y., Tong, X., & Atkinson, P. M. (2024). Filling gaps in cloudy Landsat LST product by spatial-temporal fusion of multi-scale data. *Remote Sensing of Environment*, 306, 114142. <https://doi.org/10.1016/j.rse.2024.114142>
- Wang, T., Shi, J., Ma, Y., Husi, L., Comyn-Platt, E., Ji, D., et al. (2019). Recovering land surface temperature under cloudy skies considering the solar-cloud-satellite geometry: Application to MODIS and landsat-8 data. *Journal of Geophysical Research: Atmospheres*, 124(6), 3401–3416. <https://doi.org/10.1029/2018JD028976>
- Xiao, R., Ouyang, Z., Zheng, H., Li, W., Schienke, E. W., & Wang, X. (2007). Spatial pattern of impervious surfaces and their impacts on land surface temperature in Beijing, China. *Journal of Environmental Sciences*, 19(2), 250–256. [https://doi.org/10.1016/S1001-0742\(07\)60041-2](https://doi.org/10.1016/S1001-0742(07)60041-2)
- Xu, S., Wang, D., Liang, S., Liu, Y., & Jia, A. (2023). Assessment of gridded datasets of various near surface temperature variables over Heihe River Basin: Uncertainties, spatial heterogeneity and clear-sky bias. *International Journal of Applied Earth Observation and Geoinformation*, 120, 103347. <https://doi.org/10.1016/j.jag.2023.103347>
- Yang, S., Zhang, D., Sun, L., Wang, Y., & Gao, Y. (2020). Assessing drought conditions in cloudy regions using reconstructed land surface temperature. *Journal of Meteorological Research*, 34(2), 264–279. <https://doi.org/10.1007/s13351-020-9136-4>
- Yao, R., Wang, L., Huang, X., Cao, Q., Wei, J., He, P., et al. (2023). Global seamless and high-resolution temperature dataset (GSHTD), 2001–2020. *Remote Sensing of Environment*, 286, 113422. <https://doi.org/10.1016/j.rse.2022.113422>
- Yuan, L., Li, C., Mandic, D., Cao, J., & Zhao, Q. (2019). Tensor ring decomposition with rank minimization on latent space: An efficient approach for tensor completion. *Proceedings of the AAAI Conference on Artificial Intelligence*, 33(01), 9151–9158. <https://doi.org/10.1609/aaai.v33i01.33019151>
- Zemp, M., Chao, Q., Han Dolman, A. J., Herold, M., Krug, T., Speich, S., et al. (2022). Gcos 2022 implementation plan. *Global Climate Observing System GCOS(244)*, 85.
- Zhan, W., Zhou, J., Ju, W., Li, M., Sandholt, I., Voogt, J., & Yu, C. (2014). Remotely sensed soil temperatures beneath snow-free skin-surface using thermal observations from tandem polar-orbiting satellites: An analytical three-time-scale model. *Remote Sensing of Environment*, 143, 1–14. <https://doi.org/10.1016/j.rse.2013.12.004>
- Zhang, X., Song, Y., Chen, J., & Huang, J. (2021). Landsat image-based retrieval and analysis of spatiotemporal variation of total suspended solid concentration in Jiaozhou Bay, China. *Remote Sensing*, 13(23), 4796. <https://doi.org/10.3390/rs13234796>
- Zhao, E., Gao, C., Jiang, X., & Liu, Z. (2017). Land surface temperature retrieval from AMSR-E passive microwave data. *Optics Express*, 25(20), A940–A952. <https://doi.org/10.1364/oe.25.00a940>
- Zhou, D., Xiao, J., Bonafoni, S., Berger, C., Deilami, K., Zhou, Y., et al. (2018). Satellite remote sensing of surface urban heat islands: Progress, challenges, and perspectives. *Remote Sensing*, 11(1), 48. <https://doi.org/10.3390/rs11010048>
- Zhu, X., Duan, S.-B., Li, Z.-L., Wu, P., Wu, H., Zhao, W., & Qian, Y. (2022). Reconstruction of land surface temperature under cloudy conditions from Landsat 8 data using annual temperature cycle model. *Remote Sensing of Environment*, 281, 113261. <https://doi.org/10.1016/j.rse.2022.113261>
- Zou, Z., Zhan, W., Liu, Z., Bechtel, B., Gao, L., Hong, F., et al. (2018). Enhanced modeling of annual temperature cycles with temporally discrete remotely sensed thermal observations. *Remote Sensing*, 10(4), 650. <https://doi.org/10.3390/rs10040650>